

# Changes in the Grain Boundary Character and Energy Distributions Resulting from a Complexion Transition in Ca-Doped Yttria

STEPHANIE A. BOJARSKI, SHUAILEI MA, WILLIAM LENTHE, MARTIN P. HARMER, and GREGORY S. ROHRER

The grain boundary character distribution and the relative grain boundary energy of 100 ppm Ca-doped yttria were measured before and after a previously identified grain boundary complexion transition. The grain boundary character distribution of samples exhibiting normal grain growth (before the complexion transition) favored {111} planes, whereas those exhibiting abnormal grain growth (after the complexion transition) favored {001} planes. Additionally, the relative grain boundary-to-surface energy ratios in the sample exhibiting abnormal grain growth were 33 pct lower than in the sample exhibiting normal grain growth. The results also indicate that the complexion transition increased the anisotropy of the grain boundary energy, and this may be responsible for the increase in the anisotropy of the grain boundary character distribution.

DOI: 10.1007/s11661-012-1172-y

© The Minerals, Metals & Materials Society and ASM International 2012

## I. INTRODUCTION

CONTROLLING microstructural development to obtain a theoretically dense material has been an important objective of research on yttria ceramics.<sup>[1–7]</sup> This isotropic cubic material has a large range of transparency, high melting temperature, high thermal conductivity, low thermal expansion, and corrosion resistance. Transparent yttria, in particular, is widely investigated for use as a host material for lasers<sup>[8–10]</sup> and for military applications such as infrared windows in heat-seeking rockets.<sup>[11–13]</sup> Tailoring the grain size to obtain a dense, homogenous, fine-grained microstructure is essential for optical and infrared transparency in polycrystalline ceramics. Understanding the grain boundaries in yttria will allow for more accurate control of the processes, such as grain growth<sup>[14]</sup> and sintering,<sup>[1–3,15]</sup> that influence the microstructural development and, thus, the mechanical and optical properties of the bulk ceramic.

The term “grain boundary complexion” is relatively new in microstructural science and is being used to refer to groups of grain boundaries, which are thermodynamically stable phases in their own right possessing distinct structures and compositions different from any

bulk phases.<sup>[16–23]</sup> In at least some cases, grain boundaries with different complexions can have very different properties that dominate microstructural evolution. For example, the coexistence of a high mobility and low mobility complexion in the same sample can lead to abnormal grain growth.<sup>[24]</sup> Previous work on doped aluminas has shown that a complexion transition can change both the grain boundary character distribution (GBCD) and the relative grain boundary energy.<sup>[25,26]</sup> Furthermore, it has recently been shown that the existence of a nanometer-thick intergranular film reduces the energy of the Au-alumina interface.<sup>[22]</sup> However, in the prior work, the GBCD was determined only as a function of the two grain boundary plane parameters; in this article, we examine changes in the five parameter grain boundary character distribution that are coupled to a complexion transition.

Ma<sup>[27]</sup> recently conducted a comprehensive investigation of grain growth kinetics in dense Ca and Si-doped yttria. In this study, abnormal grain growth occurred in 100 ppm Ca-doped yttria samples that were isothermally annealed in a reducing atmosphere at temperatures above 1973 K (1700 °C) and held at the annealing temperature for times longer than 0 hours. Mobility measurements paired with high-resolution transmission electron microscopy (HRTEM) and high-angle annular dark-field (HAADF) scanning transmission electron microscopy (STEM) found that the boundaries around the high-mobility grains have an amorphous intergranular film, whereas the boundaries around the slow moving grains have a lower order grain boundary complexion, which was deduced to be bilayer of adsorbed Ca. With reference to the original study of doped aluminas,<sup>[18]</sup> the film would correspond to the complexion labeled V or VI and the bilayer to the complexion labeled III. Regardless of the labels, the

---

STEPHANIE A. BOJARSKI, PhD Candidate, and GREGORY S. ROHRER, W.W. Mullins Professor and Head, are with the Department of Materials Science and Engineering, Carnegie Mellon University, Pittsburgh, PA 15213. Contact e-mail: gr20@andrew.cmu.edu SHUAILEI MA, formerly PhD Candidate, Lehigh University, Bethlehem, PA 18015, is now Product Developer with the SABIC Innovative Plastics, Pittsfield, MA 01201. WILLIAM LENTHE, Undergraduate, and MARTIN P. HARMER, Alcoa Professor, are with the Department of Materials Science and Engineering, Lehigh University.

Manuscript submitted January 11, 2012.

Article published online April 13, 2012

main point is that the boundaries have distinct structures and compositions and, therefore, different complexions. The purpose of the current article is to show that the complexion transition in 100 ppm Ca-doped yttria from an adsorbed bilayer to an amorphous film results in a reduction in the average grain boundary energy and an increase in the grain boundary energy anisotropy. The energy reduction associated with the complexion transition further supports the theory that complexions are true interface-stabilized phases in thermodynamic equilibrium with the bulk phases. It is also shown that the five-parameter GBCD is influenced by the transition and becomes more anisotropic.

The mesoscale grain boundary analysis techniques used in this study yield statistical measurements of the grain boundary character distribution and relative grain boundary energy.<sup>[28,29]</sup> Grain boundaries can be characterized by five microscopically observable parameters: three Euler angles ( $\varphi_1$ ,  $\Phi$ ,  $\varphi_2$ ) that describe the misorientation of the crystals separated by the grain boundary and two spherical coordinates ( $\varphi$ ,  $\theta$ ) that describe the normal to the plane of the grain boundary. The complete five parameter GBCD, which represents the relative area of different types of grain boundaries, can be determined by the stereological analysis of orientation maps obtained by electron backscatter diffraction (EBSD).<sup>[30–32]</sup> In this article, two types of grain boundary plane distributions will be extracted from the complete five-parameter GBCD. One type is the distribution of planes at a fixed misorientation. These distributions have the symmetry of the bicrystal and are plotted in a hemisphere. The second includes the distributions of all grain boundary planes, without regard to misorientation. These distributions have the symmetry of the crystal and are plotted in the standard stereographic triangle.

It is also possible to quantify the relative energy of a grain boundary by measuring the dihedral angle of the thermal grooves that form where grain boundaries intersect the surface. Thermal grooves form to balance the interfacial energies between the surfaces and the grain boundary. The relative energy of a grain boundary ( $\gamma_{gb}$ ) to the adjacent grain surface ( $\gamma_s$ ) can be expressed as a function of the dihedral angle ( $\Psi_s$ ) according to Eq. [1].

$$\frac{\gamma_{gb}}{\gamma_s} = 2 \cos \frac{\Psi_s}{2} \quad [1]$$

Using Mullins' analysis,<sup>[33]</sup> it is possible to measure the height and width of a thermal groove and solve for the relative interfacial energy of the grain boundary. However, this method includes several approximations and assumptions. For example, it is assumed that the two surface energies are the same, the grain boundary is normal to the surface, and the surface energy anisotropy is small. Although these assumptions will not hold for any single grain boundary, it has been found that for many measurements of grain boundary dihedral angles, the mean value and width of the distribution are reproducible and meaningful quantities.<sup>[25,34–37]</sup> In the

last decade, atomic force microscopy (AFM) has greatly simplified these measurements, and specific procedures have been established for making reliable polycrystalline grain boundary energy measurements using AFM.<sup>[37]</sup> As a result, this technique makes it possible to detect changes in the grain boundary energy that result from changes in composition or, in this case, a complexion transition.

## II. METHODOLOGY

A detailed description of the process used to produce the yttria samples can be found in Reference 27. Briefly, the samples used in the current study were hot pressed to obtain a near-theoretical density and further annealed at 1973 K (1700 °C) in a 5 pct H<sub>2</sub>-N<sub>2</sub> atmosphere with two different dwell times. The “0-hour dwell” sample was fabricated by raising the furnace temperature to 1973 K (1700 °C) and then immediately quenched. This sample had a normal grain size distribution and is referred to as NGG. The second sample was annealed at 1973 K (1700 °C) for 6 hours and then quenched. It had a bimodal or abnormal grain size distribution and is, therefore, referred to as the AGG sample. Kinetic and HRTEM analysis of the boundaries found Ca bilayers in the NGG sample (0-hour dwell) and amorphous films in the abnormal grain boundaries of the AGG sample (6-hour dwell). A kinetic analysis allowed for the assumption that the normal grain boundaries of the AGG sample also exhibited Ca bilayers.

Automated EBSD mapping data were collected for both the NGG and AGG samples on a Quanta 200 field-emission scanning electron microscope (FEI Corporation, Hillsboro, OR) with dedicated orientation imaging microscopy EDAX Delphi software configured with TSL analysis software (EDAX Inc., Mahwah, NJ). The EBSD step size for the NGG sample was 0.1  $\mu$ m on a hexagonal grid with an accelerating voltage of 10 kV. The AGG sample was imaged with a 1  $\mu$ m step size and an accelerating voltage of 20 kV when the sample had a thin Ir coating and 15 kV when the coating was removed. This coating was initially applied to eliminate charging but was found to be unnecessary; no significant differences were found in the maps of samples with or without the coating. Both samples were imaged at a working distance of 15 mm.

The images were processed before extracting the line segments using the following steps. First, a single-iteration grain dilation filter with a minimum grain size of five pixels and a tolerance of 5 deg was applied to each image. This changed 3.1 pct of the pixels in the AGG images and 7.6 pct of the pixels in the NGG images. Next, a single orientation was assigned to each grain, again with a tolerance of 5 deg. The grain boundaries were then approximated by a series of line segments with a deviation tolerance of two pixels. The process resulted in 68,116 line segments from the NGG sample and 130,087 line segments from the AGG sample. The GBCD was then calculated using open-source programs that implement a stereological procedure for determining the GBCD.<sup>[38]</sup>

Thermal grooves were produced by heating the yttria samples in an air furnace (Lindberg Furnace, Los Angeles, CA) for 30 minutes at 1573 K (1300 °C); the samples were heated to this temperature at 5 °C/min and cooled at 10 °C/min. Contact AFM topographs were recorded on these grooved samples using Solver-Next NT-MDT AFM (NT-MDT Co., Zelenograd, Moscow) and Budget Sensor ContAL-G tips (Contact mode, R-freq = 13 kHz; force constant = 0.2 N/m; Innovative Solutions Bulgaria, Ltd., Sofia, Bulgaria). The topographic images were taken with a step size of 10 nm and a 5 to 20  $\mu\text{m}$  field of view. The AFM images were edited with the open-source software Gwyddion.<sup>[39]</sup> The images were edited only if necessary. The two corrections that were sometimes applied were a plane level function to remove global tilts and, if needed, a match line correction to eliminate AFM artifacts. The dihedral angles were then determined from the widths and depths of the thermal groove, using previously described procedures.<sup>[33,35]</sup>

Topographic data along lines perpendicular to grain boundaries were measured on both the NGG and AGG samples. For the NGG sample, all the boundaries were considered equivalent. For the AGG sample, the boundaries were classified into two categories. Figure 1 shows an AFM image of the AGG sample and the corresponding topographic profiles across a boundary between a larger grain (labeled 1) and a smaller grain (labeled 2) and between two smaller grains (labeled 2 and 3). The boundaries surrounding larger grains, such as the one between grain 1 and 2, were designated as abnormal grain boundaries. The boundaries between two grains adjacent to the larger grains, such as the boundary between 2 and 3, were designated as normal grain boundaries. These were the only types of boundaries measured in the AGG sample. More than 200 boundaries were measured in each sample, and for each one, three parallel topographic traces were extracted from the images. A text file of thermal groove profiles was extracted using Gwyddion.<sup>[39]</sup> A program developed in house was then used to determine the depth and width of the groove automatically to calculate the dihedral angles, the relative energies, and the standard deviations of these quantities for each boundary. The accuracy of the program was verified by comparing its output with the values produced by a manual measurement.

### III. RESULTS

Orientation maps were measured for both the AGG and NGG yttria samples. More than 50,000 grain boundary line segments were extracted from each data set, which is sufficient to represent all grain boundary possibilities at a resolution ( $\Delta$ ) of 10 deg.<sup>[31]</sup> Grain orientation maps from the EBSD measurements, with superimposed reconstructed grain boundaries from each sample, are shown in Figure 2. The grain orientation texture in each sample is further quantified by the [001] inverse pole figures (IPF) in Figure 3.

The colors in the orientation map of the AGG sample indicates that the (111) orientation is predominately

normal to the surface, whereas the NGG sample seems to have a more random distribution. The IPFs in Figure 3 are consistent with this observation, showing that the (111)//[001] is preferred, with a peak of approximately three multiples of random distribution (MRD). The NGG sample does not have any peaks above approximately 1.5 MRD, which is consistent with the random coloring in the orientation map.

The grain boundary plane distributions of the NGG and AGG yttria samples, determined without consideration of the misorientation, are shown in Figures 4(a) and (b), respectively. The distributions are significantly different in the two samples. The NGG sample has a weak preference for {111} grain boundary planes, whereas the AGG sample favors {001} and is five times more anisotropic. It should be mentioned that the

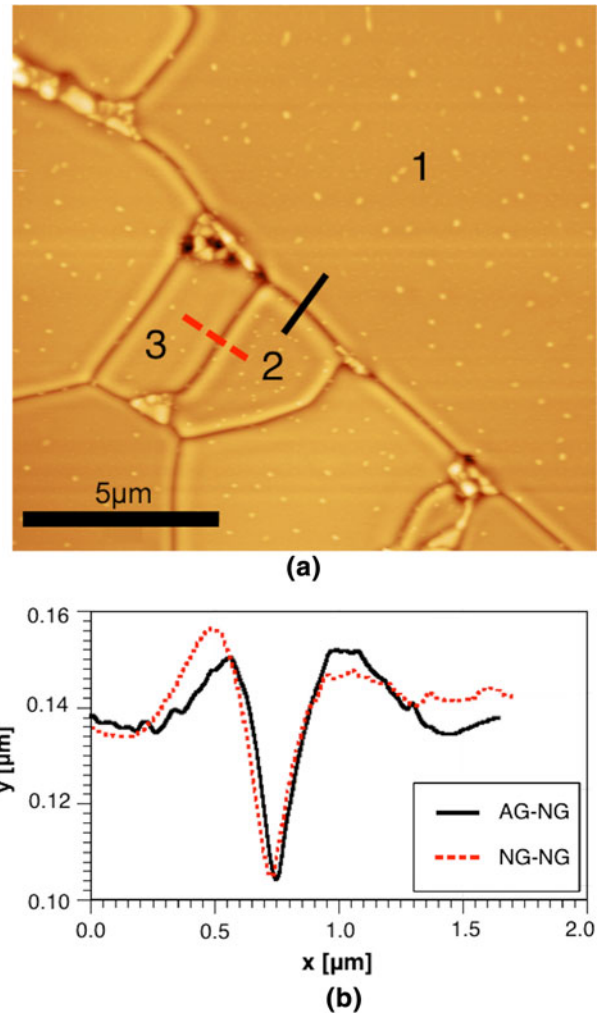


Fig. 1—(a) Topographic AFM image of the thermally grooved AGG sample, where the solid line indicates the location from which the topographic data in (b) was extracted across an abnormal grain boundary and the dashed line indicates the source of the data from the adjacent normal boundary. (b) In the corresponding grain boundary topographs, the height of the boundary is on the vertical axis and width on the horizontal axis. The solid line corresponds to the solid line across the abnormal boundary scan line in (a). Similarly, the dashed line corresponds to the topographic data across the normal grain boundary.

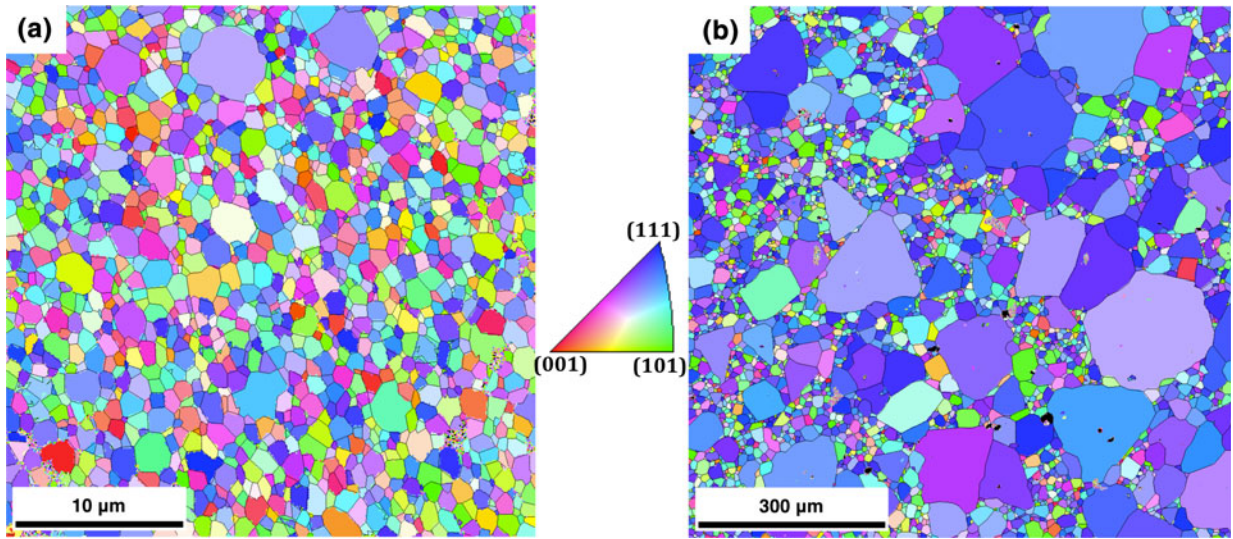


Fig. 2—Inverse pole figure maps from EBSD data with superimposed reconstructed grain boundaries for (a) NGG sample, which exhibits a homogeneous grain size distribution, and (b) AGG sample, displaying a bimodal grain size distribution and an apparent change in texture.

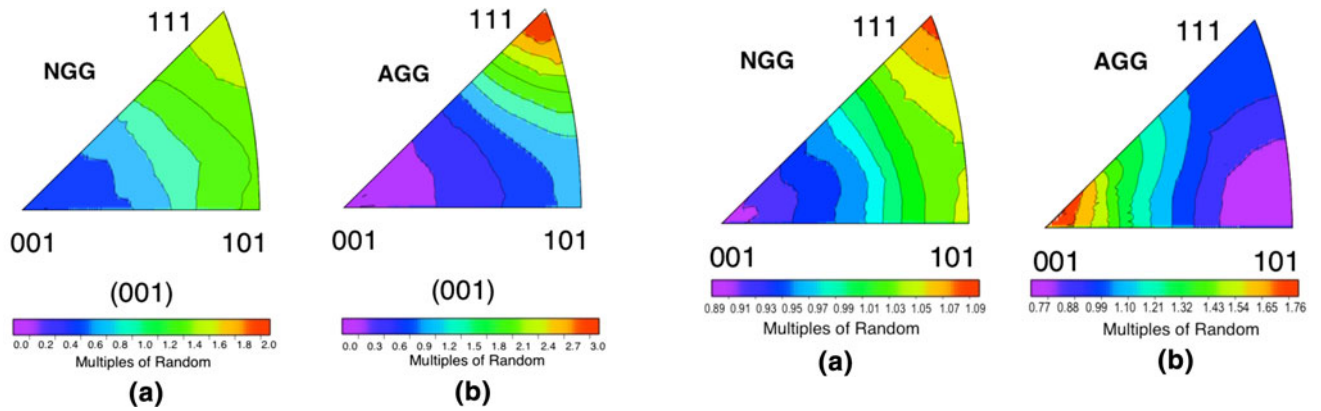


Fig. 3—Inverse pole figures for the [001] sample reference direction. (a) The NGG sample lacks significant texture. (b) The AGG sample shows a preference for {111} orientations.

difference in texture could influence the calculated grain boundary plane distribution.<sup>[32]</sup> In particular, the result from the AGG sample will have some bias because of the nonrandom orientation distribution. However, the (111) texture in the AGG sample would, if anything, lead to an overestimation of the population of (111) planes. Therefore, the observation that (100) planes are dominant is not an artifact of the texture.

The stereographic projections in Figures 5 through 7 show the distributions of grain boundary planes at specific misorientations. The most notable peak in the distributions of both the NGG and AGG samples is the twist grain boundary at 45 deg/[100], terminated by (100) and (100) planes. The maximum at the twist position is approximately four MRD for the NGG sample and 5.1 MRD in the AGG sample (Figure 5). In the AGG sample, 30 deg/[110] shows a high population of (001) and (112) asymmetric tilt boundaries (Figure 6). These grain boundaries are not highly populated at the same misorientation for the NGG sample. Additionally, the

Fig. 4—The grain boundary plane distributions, independent of misorientation, for the (a) NGG sample and (b) the AGG sample plotted in the standard stereographic triangle.

60 deg/[111] NGG distribution shows a broad peak in the vicinity of the (111) twist boundary, whereas the AGG distribution shows a shift in the distribution with high populations at all of the {001} and {111} planes (Figure 7). All three of these misorientations show a significant change in the anisotropy of the grain boundary character between the NGG and AGG sample. Additionally, the occurrence of increased grain boundary populations at {100} orientations in the grain boundary plane distributions at specific misorientations for the AGG samples is consistent with the shift from {111} to {100} in the two-parameter grain boundary plane distributions of the NGG and AGG samples (Figure 4).

AFM images were used to measure the topography of the grain boundary thermal grooves on both samples. Figure 1(a) shows an example of an AGG topographic AFM image and the corresponding topography along a single line that crosses the abnormal grain boundary separating crystals 1 and 2 and the adjacent normal grain boundaries separating crystals 2 and 3. The boundaries adjacent to the abnormal grains were the

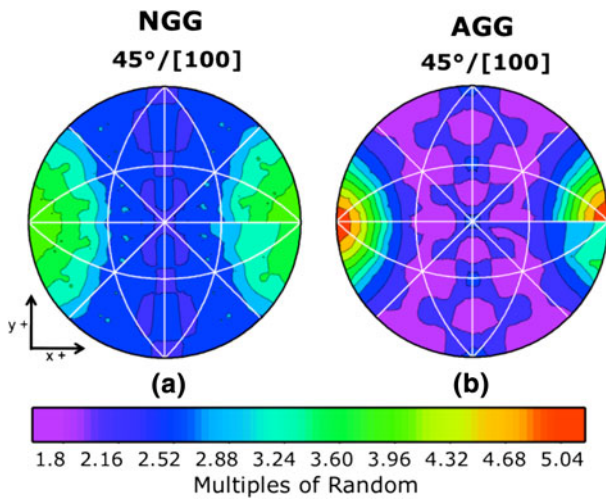


Fig. 5—Grain boundary plane distributions for the misorientation of 45 deg around [100], plotted in stereographic projection, with the [100] direction orientated horizontally to the right and the [001] direction is normal to the figure. Subsequent figures are plotted in the same way: (a) NGG sample and (b) AGG sample.

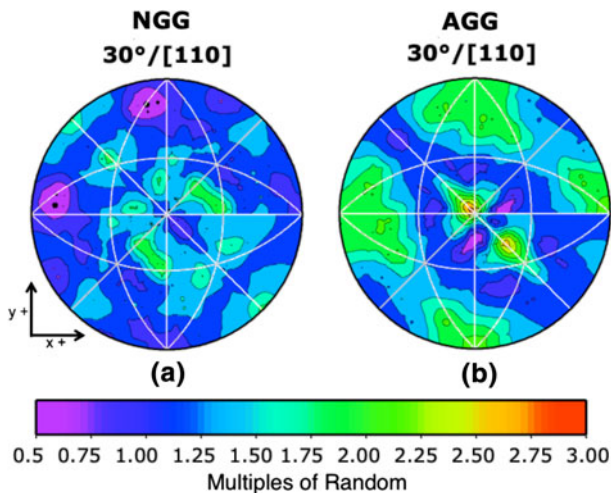


Fig. 6—Grain boundary plane distributions for the misorientation of 30 deg around [110]: (a) NGG sample and (b) AGG sample.

only normal grain growth boundaries analyzed in the AGG sample; this was done as an attempt to keep the local chemistry near the boundaries consistent. Similar topographic data were obtained for lines across boundaries with well-defined grooves in the NGG sample. Figure 1(b) shows an example of topographic data from the AGG that corresponds to the line profiles across the grain boundaries indicated on Figure 1(a).

The cumulative distribution function of the dihedral angles for the abnormal grain boundaries (AG-NG), normal grain boundaries in the AGG sample (NG-NG), and NGG grain boundaries (NGG) are shown in Figure 8. The average values of the dihedral angle and relative interfacial energy for each boundary type are tabulated in the inset. It was found that the NGG sample had an average relative interfacial energy of 0.42. The average interfacial energy for the abnormal and

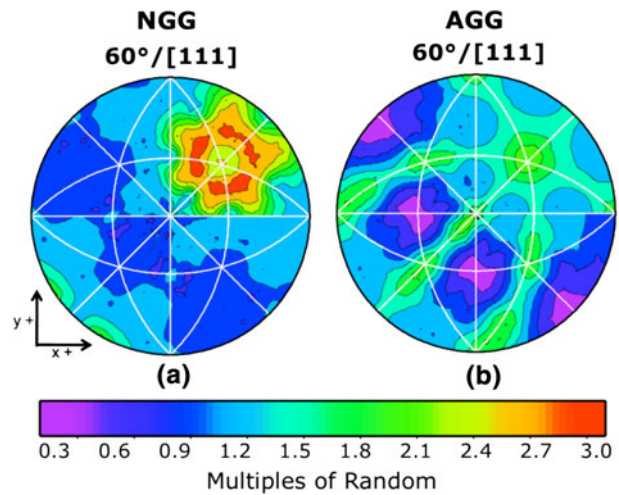


Fig. 7—Grain boundary plane distributions for the misorientation of 60 deg around [111]: (a) NGG sample and (b) AGG sample.

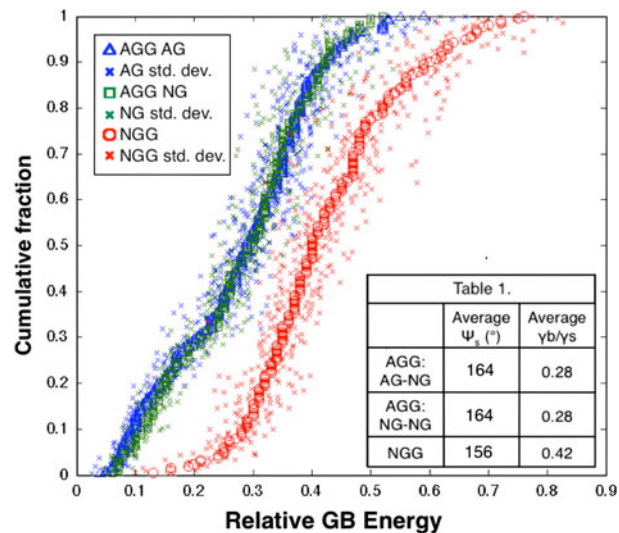


Fig. 8—Cumulative distribution function comparing relative grain boundary energies for abnormal grain boundaries (triangle), normal boundaries in AGG sample (square), and normal boundaries in NGG sample (circle).

normal grain boundaries in the AGG sample is 0.28, corresponding to a 33 pct reduction in energy between the NGG and AGG sample.

#### IV. DISCUSSION

The five-parameter GBCD of 100 ppm Ca-doped yttria can be compared with previous measurements of the GBCD of undoped yttria reported by Dillon and Rohrer.<sup>[40]</sup> Of the two samples considered here, the GBCD of the NGG sample was most similar to that of the undoped sample. However, one significant difference between the two distributions was found at the 45 deg/[100] misorientation. For the 100 ppm Ca-doped samples, the twist boundary at this misorientation is the

maximum of the distribution (Figure 5(b)), whereas it was a minimum in the undoped sample. In the past, impurities have been shown to influence grain boundary plane distributions,<sup>[41]</sup> and in this case, the higher population of the {100} type planes for the 45 deg/[100] twist boundaries could be caused by the Ca impurities. Additionally, the change from a preference for {111} planes in the grain boundary plane distribution of the NGG sample (Figure 4(a)) to {001} for the AGG sample (Figure 4(b)) is consistent with the stabilization of {001} planes by Ca. The preference for a specific grain boundary plane orientation caused by the addition of segregating impurities is one cause of the observed increase in GBCD anisotropy.

The results show that there are significant differences in the GBCD of the NGG and AGG sample. This finding is consistent with results from several doped aluminas reported by Dillon *et al.*,<sup>[26]</sup> who showed that complexion transitions altered the two-parameter grain boundary plane distributions. Analogous to the current study, the change in the grain boundary plane distribution was accompanied by an increase in the anisotropy of the distribution. In the current work, the samples differ only in the amount of time that they were annealed at 1973 K (1700 °C), and the changes in the GBCD are also attributed to a complexion transition. Based on the work of Ma,<sup>[27]</sup> who studied the same Ca-doped yttria samples, the slower moving grain boundaries have a bilayer of Ca and the faster moving boundaries have an intergranular film. It is assumed that all the boundaries in the NGG sample have the bilayer complexion, and in the AGG sample, the boundaries around the largest grains have the intergranular film and the boundaries around the smaller grains have the bilayer complexion. The coexistence of two grain boundary complexions resulted in the abnormal grain growth in the AGG sample. It has been established by studies of other systems that the GBCD is inversely correlated to the grain boundary energy distribution.<sup>[29]</sup> Therefore, the changes in the GBCD observed in this study are presumably associated with changes in the grain boundary energy that are associated with the complexion transition. This idea is supported by the results of the thermal groove analysis.

The results in Figure 8 clearly show that the relative energies of grain boundaries in the sample with abnormal grains are lower than in the sample without abnormal grains. Furthermore, the width of the relative energy distribution is larger in the AGG sample than in the NGG sample. In the former, the maximum and minimum energy of the distribution are separated by a factor of ten, whereas in the latter, the maximum and minimum of the distribution are separated by only a factor of six. Assuming that the inverse correlation of the GBCD with the grain boundary energy observed in other systems also applies in this study, the result is consistent with the finding that the anisotropy of the GBCD is larger in the AGG sample. This finding is also consistent with previous results from doped aluminas, which showed both an increase in anisotropy and, in some cases, a reduction in the relative boundary energy.<sup>[25]</sup> In the previous work, the measured grain boundary energy

did not decrease in every case that was tested, and one explanation for this is that the energy measurements are made long after the complexion transition has occurred; they do not necessarily reflect the energy at the time of the transition. Boundaries may be metastable and change their composition and energy over time. In the current case, where samples of the same composition were heated at the same temperature, we must assume that the bilayer complexion is metastable with respect to the intergranular film because more boundaries transform to the higher mobility complexion with time.

The nucleation of complexion transitions is currently not understood. Earlier work has shown that the transitions are activated and metastable complexions can be found together with stable complexions.<sup>[42]</sup> One possibility is that the complexion transition nucleates preferentially on the highest energy grain boundaries. Although this would remove some higher energy grain boundaries from the system, it also creates lower energy boundaries and the overall effect is that the anisotropy of the energy increases. In this case, the (100) oriented planes are stabilized and presumably have the lowest energy. This is observed in both the misorientation averaged grain boundary plane distribution and in the distribution of grain boundary planes at individual misorientations.

One unexpected result is that the average energies of the normal and abnormal boundaries in the AGG sample are the same. Furthermore, the width and shape of the two distributions are also the same. It was initially assumed that the normal grain boundaries in the AGG sample had the same complexion as the grain boundaries in the NGG sample. Therefore, it was expected that the energy distribution of the boundaries around the small grains in the AGG sample would be similar to the energy distribution of the NGG sample. This was not the case. The most likely reason is that the complexion transition occurred continuously throughout the 6-hour anneal, and by the end, all the boundaries had transformed. If the complexion transition nucleated on the highest energy boundaries first, near the beginning of the anneal, then they have a mobility advantage for a longer time and grow larger compared with the others. As the annealing time continues, other lower energy boundaries complete the complexion transition until all boundaries are transformed. However, at this point, there is no mobility advantage and the early transforming grains are already much larger than the late transforming grains. We are currently testing this idea by grain growth simulations. Alternatively, it might be suggested that a second round of complexion transitions may have occurred during the thermal grooving cycle, which was at a lower temperature and in an oxidizing atmosphere. However, considering that this heat treatment was the same for both samples, it is difficult to understand why the outcome would be so different. Although the reason for this unexpected result is not known with certainty, it is clear that boundaries in the NGG and AGG samples have different population distributions, energies, and complexions.

As a final point, it was observed that the AGG sample, with lower energy grain boundaries, exhibited a stronger texture than the NGG sample. It should be

noted that after annealing, the surface layer was removed by polishing so the large grains visible in the images could not have benefitted from a surface energy advantage. In previous studies of alumina, no changes in texture were associated with complexion transitions, and the mechanism by which texture increases is not obvious in this study. However, it is not unusual for hot pressing to create texture, and this is likely the source of the (111)//[001] texture in the AGG sample. Because the texture is mostly associated with the larger crystals whose surrounding boundaries transformed to the higher order complexion at an earlier time, one may speculate that nonuniform residual stresses induced by the hot pressing may promote the nucleation of complexion transitions on grains of a specific orientation. If that were the case, then it would provide a new mechanism for the control of interface kinetics and microstructure development.

## V. CONCLUSIONS

Ca-doped yttria samples of the same composition, sintered at the same temperature but held for different times, have significantly different grain boundary character distributions and mean grain boundary energies. Abnormal grain growth at longer annealing times initiated a clear shift in the population of grain boundary planes from a weak {111} preference to a stronger {001} preference. This indicates that the complexion transitions influence the relative interfacial energies. The AFM thermal groove analysis showed that the grain boundaries in the sample with abnormal grain growth had energies that were, on average, 33 pct lower than in the sample without abnormal grain growth. The complexion transition leading to abnormal grain growth may be attributed to this reduction in energy. The results presented in this study are consistent with the idea that the complexion transition altered the grain boundary energy anisotropy, and this led to a change in the mesoscale grain boundary character distribution.

## ACKNOWLEDGMENTS

G.R. and S.B. acknowledge MRSEC program of the National Science Foundation under Award Number DMR-0520425. W.L. acknowledges the National Science Foundation Research Experience for Undergraduates Site grant DMR-1005076. M.P.H. and S.M. gratefully acknowledge the financial support from the U.S. DOE Office of Basic Energy Science grant in the Electron and Scanning Probe Microscopies Program (Grant No. DE-FG02-08ER46548) managed by Dr. Jane G. Zhu.

## REFERENCES

1. L. Borovkova, E. Lukin, D. Poluboyarinov, and E. Sapozhnikova: *Refract. Ind. Ceram.*, 1970, vol. 11, pp. 717–22.
2. L.B. Borovkova, E.S. Lukin, and D.N. Poluboyarinov: *Refract. Ind. Ceram.*, 1972, vol. 13, pp. 595–600.
3. P.L. Chen and I.W. Chen: *J. Am. Ceram. Soc.*, 1996, vol. 79, pp. 1801–09.
4. P. Duran, J. Tartaj, and C. Moure: *Ceram. Int.*, 2002, vol. 28, pp. 791–803.
5. P.J. Jorgensen and R.C. Anderson: *J. Am. Ceram. Soc.*, 1967, vol. 50, pp. 553–58.
6. S.L. Ma and M.P. Harmer: *J. Am. Ceram. Soc.*, 2011, vol. 94, pp. 651–55.
7. Y. Tsukuda: *Am. Ceram. Soc. Bull.*, 1983, vol. 62, pp. 510–12.
8. A. Brenier and G. Boulon: *J. Alloys Compd.*, 2001, vol. 323, pp. 210–13.
9. C. Greskovich and J.P. Chernoch: *J. Appl. Phys.*, 1974, vol. 45, pp. 4495–4502.
10. J.R. Lu, K. Takaichi, T. Uematsu, A. Shirakawa, M. Musha, K. Ueda, H. Yagi, T. Yanagitani, and A.A. Kaminskii: *Jpn. J. Appl. Phys. Part 2-Lett.*, 2002, vol. 41, pp. L1373–75.
11. P. Hogan, T. Stefanik, C. Willingham, and R. Gentilman: *The 10th DoD Electromagnetic Windows Symp*, Norfolk, VA, 2004.
12. G.C. Wei, M.R. Pasucci, E.A. Trichett, C. Brecher, and W.H. Rhodes: *Ceramics and Inorganic Crystals for Optics, Electro-Optics, and Nonlinear Conversion*, San Diego, CA, 1988, pp. 5–13.
13. K.A. Wickershshem and R.A. Lefever: *J. Opt. Soc. Am.*, 1961, vol. 51, pp. 1147–48.
14. J.E. Burke and D. Turnbull: *Progr. Met. Phys.*, 1952, vol. 3, pp. 220–92.
15. R.L. Coble: *J. Appl. Phys.*, 1961, vol. 32, pp. 793–99.
16. S.J. Dillon, M.P. Harmer, and J. Luo: *JOM*, 2009, vol. 61, pp. 38–44.
17. S.J. Dillon, M. Tang, W.C. Carter, and M.P. Harmer: *Acta Mater.*, 2007, vol. 55, pp. 6208–18.
18. M.P. Harmer: *J. Am. Ceram. Soc.*, 2010, vol. 93, pp. 301–17.
19. M.P. Harmer: *Science*, 2011, vol. 332, pp. 182–83.
20. M. Tang, W.C. Carter, and R.M. Cannon: *Phys. Rev. B*, 2006, vol. 73, p. 14.
21. M. Tang, W.C. Carter, and R.M. Cannon: *Phys. Rev. Lett.*, 2006, vol. 97, p. 4.
22. M. Baram, D. Chatain, and W.D. Kaplan: *Science*, 2011, vol. 332, pp. 206–09.
23. J. Luo, H.K. Cheng, K.M. Asl, C.J. Kiely, and M.P. Harmer: *Science*, 2011, vol. 333, pp. 1730–33.
24. S.J. Dillon and M.P. Harmer: *Acta Mater.*, 2007, vol. 55, pp. 5247–54.
25. S.J. Dillon, M.P. Harmer, and G.S. Rohrer: *J. Am. Ceram. Soc.*, 2010, vol. 93, pp. 1796–1802.
26. S.J. Dillon, H. Miller, M.P. Harmer, and G.S. Rohrer: *Int. J. Mater. Res.*, 2010, vol. 101, pp. 50–56.
27. S. Ma. Ph.D. Dissertation, Lehigh University, Bethlehem, PA, 2010.
28. G.S. Rohrer: *J. Am. Ceram. Soc.*, 2011, vol. 94, pp. 633–46.
29. G.S. Rohrer: *J. Mater. Sci.*, 2011, vol. 46, pp. 5881–95.
30. G.S. Rohrer, D.M. Saylor, B. El Dasher, B.L. Adams, A.D. Rollett, and P. Wynblatt: *Z. Fur Metallkunde*, 2004, vol. 95, pp. 197–214.
31. D.M. Saylor, B.S. El-Dasher, B.L. Adams, and G.S. Rohrer: *Metall. Mater. Trans. A*, 2004, vol. 35A, pp. 1981–89.
32. D.M. Saylor and G.S. Rohrer: *J. Am. Ceram. Soc.*, 2002, vol. 85, pp. 2799–2804.
33. W.W. Mullins: *J. Appl. Phys.*, 1957, vol. 28, pp. 333–39.
34. S.J. Dillon, M.P. Harmer, and G.S. Rohrer: *Acta Mater.*, 2010, vol. 58, pp. 5097–5108.
35. C.A. Handwerker, J.M. Dynys, R.M. Cannon, and R.L. Coble: *J. Am. Ceram. Soc.*, 1990, vol. 73, pp. 1371–77.
36. D.M. Saylor, A. Morawiec, B.L. Adams, and G.S. Rohrer: *Interface Sci.*, 2000, vol. 8, pp. 131–40.
37. D.M. Saylor and G.S. Rohrer: *J. Am. Ceram. Soc.*, 1999, vol. 82, pp. 1529–36.
38. G.S. Rohrer: [http://mimp.materials.cmu.edu/~gr20/stereology/100601\\_stereo.zip](http://mimp.materials.cmu.edu/~gr20/stereology/100601_stereo.zip). 2011.
39. Gwyddion, <http://gwyddion.net/resources.php>. 2011.
40. S.J. Dillon and G.S. Rohrer: *J. Am. Ceram. Soc.*, 2009, vol. 92, pp. 1580–85.
41. F. Papillon, G.S. Rohrer, and P. Wynblatt: *J. Am. Ceram. Soc.*, 2009, vol. 92, pp. 3044–51.
42. S.J. Dillon and M.P. Harmer: *J. Eur. Ceram. Soc.*, 2008, vol. 28, pp. 1485–93.